CZECH TECHNICAL UNIVERSITY IN PRAGUE

Faculty of Electrical Engineering

Department of Power Engineering

Polarizability of electrically small perfectly conducting scatterers

Master Thesis

Study Programme: Electrical Engineering, Power Engineering and Management

Branch of study: Electrical Power Engineering

Supervisor: doc. Ing. Lukáš Jelínek, Ph.D.

Bc. Ondřej Krátký

Prague 2016

České vysoké učení technické v Praze
Fakulta elektrotechnická

katedra elektroenergetiky

ZADÁNÍ DIPLOMOVÉ PRÁCE

Student: **Ondřej Krátký**

Studijní program: Elektrotechnika, energetika a management
Obor: Elektroenergetika

Název tématu: **Polarizovatelnost elektricky malých dokonale vodivých objektů**

Pokyny pro vypracování:

Navrhněte možnost výpočtu čtyř tenzorů dipólové polarizovatelnosti [1-3] elektricky malých dokonale vodivých objektů libovolného tvaru. Metodu formulujte tak, aby byla kompatibilní s diskretizačním schématem Rao-Wilton-Glisson (RWG) [4] a s řešením elektromagnetic kého pole pomocí integrálních rovnic a metody momentů. Prozkoumejte zejména možnost využití maticové reprezentace spojitých operátorů v RWG bázi a navrhněte vhodné ozáření polarizovaného objektu. Získané algoritmy ověřte na kanonických příkladech (koule, disk, krychle), kde jsou výsledné hodnoty známy. Prozkoumejte přesnost výpočtu s ohledem na kvalitu diskretizační mříže, elektrickou velikost polarizovaného objektu a na přítomnost hran.

Seznam odborné literatury:

[1] A. Ishimaru, S. W. Lee, Y. Kuga, V. Jandhyala, "Generalized Constitutive Relations for Metamaterials Based on the Quasi-Static Lorentz Theory", IEEE Trans. Antennas Propag., Vol. 51, pp. 2550-2557, 2003.
[2] R. E. Collin, Field Theory of Guided Waves, John Wiley - IEEE Press, 1990.
[3] S. Tretyakov, Analytical Modeling in Applied Electromagnetics, Artech House, 2002.
[4] S. M. Rao, D. R. Wilton, and A. W. Glisson, "Electromagnetic scattering by surfaces of arbitrary shape", IEEE Trans. Antennas Propag., Vol. 30, pp. 409–418, 1982.

Vedoucí: doc. Lukáš Jelínek Ing., Ph.D.

Platnost zadání: do konce zimního semestru 2017/2018

L.S.

doc. Ing. Zdeněk Müller, Ph.D.
vedoucí katedry

prof. Ing. Pavel Ripka, CSc.
děkan

V Praze dne 18. 4. 2016

Anotace

Tato diplomová práce je zaměřena na výpočet tenzorů polarizovatelnosti. Úvod se věnuje představení konceptu polarizovatelnosti a jejímu využití. První část diplomové práce se zabývá odvozením vztahů pro výpočet těchto tenzorů. V druhé části je představena implementace těchto vztahů v prostředí MATLAB a následné porovnání výsledků s jinými autory.

Klíčová slova

Tenzory polarizovatelnosti, elektricky malé objekty, Rao-Wilton-Glisson báze, rovnice pro elektrické pole v integrálním tvaru, impedanční matice.

Summary

This diploma thesis is focused on the calculation of polarizability tensors. Introduction is focused on the description of the polarizability tensors and their usage. The first part of the diploma thesis derives relations necessary to calculate the polarizability tensors. The second part is focused on the implementation of these relations in MATLAB and comparison of obtained results with different authors.

Keywords

Polarizability tensors, electrically small scatterers, Rao-Wilton-Glisson basis, electric field integral equation, impedance matrix.

Čestné prohlášení

Prohlašuji, že jsem předloženou práci vypracoval samostatně, a že jsem uvedl veškeré použité informační zdroje v souladu s Metodickým pokynem o dodržování etických principů při přípravě vysokoškolských závěrečných prací.

V Praze dne 26. 5. 2016 Bc. Ondřej Krátký

Poděkování

Tímto děkuji doc. Ing. Lukáši Jelínkovi Ph.D. a Ing. Miloslavu Čapkovi Ph.D. za konzultace a pomoc při vypracování mé diplomové práce. Také děkuji své rodině za podporu při studiu a tvorbě této diplomové práce.

Content

List of figures

List of tables

List of symbols

ε	permittivity
ε_0	vacuum permittivity
μ	permeability
μ_0	vacuum permeability
Z_0	impedance of vacuum
c_0	speed of light in vacuum
a	radius of the smallest sphere which completely surrounds the object
V_0	volume of the smallest sphere which completely surrounds the object
k	wave number
f	frequency
ω	angular frequency
ka	electric size
$\boldsymbol{\alpha}$	polarizability tensor
$\boldsymbol{\alpha}_{ee}$	electric polarizability tensor
$\boldsymbol{\alpha}_{mm}$	magnetic polarizability tensor
$\boldsymbol{\alpha}_{em}$	electro-magnetic polarizability tensor
$\boldsymbol{\alpha}_{me}$	magneto-electric polarizability tensor
Ω	geometrical object
$\boldsymbol{E}(\boldsymbol{r})$	incident electric field
$\boldsymbol{B}(\boldsymbol{r})$	incident magnetic induction
$\boldsymbol{p}$	electric dipole moment of a scatterer
$\boldsymbol{m}$	magnetic dipole moment of a scatterer
$\mathbf{P}$	electric dipole moment matrix
T	triangle
$\mathbf{M}$	magnetic dipole matrix
$\mathbf{F}$	feeding matrix
$\mathbf{Q}$	excitation matrix
$\mathbf{I}$	vector of current expansion coefficients
$\mathbf{C}$	centre of a triangle
$\mathbf{V}$	vertex of a triangle
A	area of a triangle
$\boldsymbol{\rho}$	vector describing the RWG basis
$\boldsymbol{r}$	radius vector

N	number of triangles
$\boldsymbol{K}(\boldsymbol{r})$	surface current density
l	length of an RWG edge of a triangle
j	imaginary unit
$\mathbf{Z}$	impedance matrix
$\mathbf{\Sigma}$	loss matrix
$\mathbf{U}$	identity matrix
J_n	Bessel's function of the first kind and order n
δ	penetration depth
$\boldsymbol{f}(\boldsymbol{r})$	basis function

List of abbreviations

BCSRR	broadside-coupled split ring resonator
BW	Bessel's wave
EFIE	electric field integral equation
GUI	graphical user interface
PEC	perfect electric conductor
PW	plane wave
RWG	Rao-Wilton-Glisson

1. Introduction

The interest of scientists and engineers in scattering properties of electrically small objects and in evaluation of their polarizability tensors accompany the electromagnetic theory from its very beginning [1], [2]. The polarizability tensors are an indispensable tool for designing artificial materials [3] and frequency selective surfaces [4]. Thanks to the relation of the polarizability tensors to the radar cross-section [5] of a scatterer and to the radiation quality factor [6], the polarizability tensors also well describe the radiation properties of electrically small antennas. The precise evaluation of the polarizability tensors is thus of major interest for many branches of applied electromagnetism.

In canonical cases, there exist analytical models for polarizability tensors [7], [8]. Unfortunately, realistic scatters have complex geometry and their polarizability tensors can only be extracted through numerical methods or measurements. In the current state-of-art, there are many numerical implementations available, see [9], [10] and the references there in. Existing methods however commonly operate in static limit [9], ignore losses and magneto-electric tensors and very importantly lack freely available codes for polarizability tensors evaluation. As for the polarizability measurements, the pioneering work has been done Cohn [11], in which the scatterer is placed in an electrolyte. For recent methods, which use the vacuum environment, we mention [12], [13] which obtain the particle polarizability from a measurement of the scattering parameters of a waveguide segment loaded by the analysed body or [14] which uses a measurement of the scattering parameters of a two-dimensional square array of analysed bodies. All the aforementioned methods are however able to measure only some components of the polarizability tensors and assume highly restrictive symmetries of analysed bodies.

In this thesis, we propose and verify general method for extraction of all four polarizability tensors of arbitrarily shaped bodies with finite conductivity. The presented scheme uses full-wave numerical evaluation, automatically accounting for ohmic and radiation losses. The thesis also discusses the implementation of this method in the Rao-Wilton-Glisson basis [15], which results in a freely available code.

2. Definition of polarizability tensors

This Chapter briefly introduces the polarizability concept. Let us assume an electrically small scatterer, which is fully enclosed in a sphere of radius a $(ka \ll 1)$ centred in the coordinate system with k being the free space wave number [16]. Under the assumption of time-harmonic steady state [16] $F(t) = \mathrm{Re}\{F(\omega)\exp(\mathrm{j}\omega t)\}$ with angular frequency ω, the illumination of a standalone scatterer by an incident electromagnetic wave with electric field $\boldsymbol{E}^{[3\times1]}(\boldsymbol{r})$ and magnetic field $\boldsymbol{B}^{[3\times1]}(\boldsymbol{r})$ gives rise to an electric and a magnetic dipole moments $\boldsymbol{p}^{[3\times1]}, \boldsymbol{m}^{[3\times1]}$ according to [1]

$$\begin{pmatrix} \boldsymbol{p} \\ \boldsymbol{m} \end{pmatrix} = \boldsymbol{\alpha} \begin{pmatrix} \boldsymbol{E}(0) \\ \boldsymbol{B}(0) \end{pmatrix}, \qquad \boldsymbol{\alpha} = \begin{pmatrix} \boldsymbol{\alpha}_{\mathrm{ee}} & \boldsymbol{\alpha}_{\mathrm{em}} \\ \boldsymbol{\alpha}_{\mathrm{me}} & \boldsymbol{\alpha}_{\mathrm{mm}} \end{pmatrix}, \tag{2.1}$$

where $\boldsymbol{\alpha}_{\mathrm{ee}}^{[3\times3]}$, $\boldsymbol{\alpha}_{\mathrm{mm}}^{[3\times3]}$, $\boldsymbol{\alpha}_{\mathrm{em}}^{[3\times3]}$ and $\boldsymbol{\alpha}_{\mathrm{me}}^{[3\times3]}$ are the second order polarizability tensors [7], [8]. The electric and magnetic fields are generally changing in the space but, under the assumption of electrically small size, they can be considered constant in the volume of the scatterer. The field at origin $\boldsymbol{E}(0)$ and $\boldsymbol{B}(0)$ is used as a reasonable approximation, since the scatterer is centred at the origin of the coordinate system.

Under the assumption of a scatterer made of highly conductive material, the electric and the magnetic dipole moments, needed for (2.1), can be evaluated from the knowledge of the induced surface current density $\boldsymbol{K}(\boldsymbol{r})$ as

$$\boldsymbol{p} = \frac{1}{\mathrm{j}\omega}\int_S \boldsymbol{K}(\boldsymbol{r})\,\mathrm{d}S, \tag{2.2}$$

$$\boldsymbol{m} = \frac{1}{2}\int_S \boldsymbol{r}\times\boldsymbol{K}(\boldsymbol{r})\,\mathrm{d}S. \tag{2.3}$$

Notice that the polarizability tensor $\boldsymbol{\alpha}$ fully characterizes the scattering properties of an electrically small scatterer [9], [8]. The main topic of this thesis is a calculation of $\boldsymbol{\alpha}$ of a solitary and highly conducting scatterer.

3. Excitation of polarizability tensors

This Chapter demonstrates how the polarizability tensor $\boldsymbol{\alpha}$ can be evaluated. The derivation starts with imagining six different excitation scenarios

$$\mathbf{F} = \begin{bmatrix} \boldsymbol{E}_1(0) & \cdots & \boldsymbol{E}_6(0) \\ \boldsymbol{B}_1(0) & & \boldsymbol{B}_6(0) \end{bmatrix}, \tag{3.1}$$

producing six different polarizations of the scatterer according to (2.1). If these excitations are chosen as to make the columns of the feeding matrix **F** linearly independent, the polarizability tensors can be evaluated as

$$\begin{bmatrix} \boldsymbol{\alpha}_{\mathrm{ee}} & \boldsymbol{\alpha}_{\mathrm{em}} \\ \boldsymbol{\alpha}_{\mathrm{me}} & \boldsymbol{\alpha}_{\mathrm{mm}} \end{bmatrix} = \begin{bmatrix} \boldsymbol{p}_1 & \cdots & \boldsymbol{p}_6 \\ \boldsymbol{m}_1 & & \boldsymbol{m}_6 \end{bmatrix} \mathbf{F}^{-1}. \tag{3.2}$$

The next step is the evaluation of the surface current density $\boldsymbol{K}(\boldsymbol{r})$ needed for (2.2) and (2.3). Throughout this thesis, $\boldsymbol{K}(\boldsymbol{r})$ is obtained from the electric field integral equation (EFIE) (see Appendix 7.1) [17], discretized in a given basis

$$\boldsymbol{K}(\boldsymbol{r}) = \sum_n I_n \boldsymbol{f}_n(\boldsymbol{r}), \tag{3.3}$$

where $\mathbf{I}^{[N\times 1]}$ is the vector of expansion coefficients with unit $\left[\mathrm{A}\cdot\mathrm{m}^{-1}\right]$ and $\boldsymbol{f}_n(\boldsymbol{r})$ is a suitable dimensionless basis function.

The expansion (3.3) transforms the EFIE into [17] (it is shown for all six incident waves)

$$\left(\mathbf{\Sigma}-\mathbf{Z}\right)\left[\mathbf{I}_1 \quad \cdots \quad \mathbf{I}_6\right]=\mathbf{Q}=\begin{bmatrix}\left\langle \boldsymbol{f}_1,\boldsymbol{E}_1\right\rangle \cdots \left\langle \boldsymbol{f}_1,\boldsymbol{E}_6\right\rangle \\ \vdots \quad \ddots \quad \vdots \\ \left\langle \boldsymbol{f}_N,\boldsymbol{E}_1\right\rangle \cdots \left\langle \boldsymbol{f}_N,\boldsymbol{E}_6\right\rangle\end{bmatrix}, \tag{3.4}$$

with $\mathbf{Q}^{[N\times 6]}$ as an excitation matrix with unit $\left[\mathrm{V}\cdot\mathrm{m}\right]$, $\mathbf{Z}^{[N\times N]}$ as the well-known impedance matrix [17], with $\mathbf{\Sigma}^{[N\times N]}$ as the matrix representing ohmic losses of a lossy conductor and with

$$\left\langle \boldsymbol{f},\boldsymbol{g}\right\rangle=\int_S \boldsymbol{f}^{*}\left(\boldsymbol{r}\right)\cdot\boldsymbol{g}\left(\boldsymbol{r}\right)\mathrm{d}S \tag{3.5}$$

as the scalar product. The construction of the matrices $\mathbf{Z}$ and $\mathbf{\Sigma}$ is detailed in Appendices 7.6 and 7.7.

Substitution of (3.3) into (2.2), (2.3) and utilization of (3.4) allow us to write

$$\begin{bmatrix}\boldsymbol{p}_1 & \cdots & \boldsymbol{p}_6\\ \boldsymbol{m}_1 & & \boldsymbol{m}_6\end{bmatrix}=\begin{bmatrix}\mathbf{P}\\ \mathbf{M}\end{bmatrix}\left[\mathbf{I}_1 \quad \cdots \quad \mathbf{I}_6\right]=\begin{bmatrix}\mathbf{P}\\ \mathbf{M}\end{bmatrix}\left(\mathbf{\Sigma}-\mathbf{Z}\right)^{-1}\mathbf{Q}, \tag{3.6}$$

where matrices $\mathbf{P}^{[3\times N]},\mathbf{M}^{[3\times N]}$ are representations of (2.2) and (2.3) in the basis (3.3). The construction of matrices **P** and **M** is detailed in Appendices 7.4 and 7.5.

Putting all together, we have

$$\begin{bmatrix}\boldsymbol{\alpha}_{\mathrm{ee}} & \boldsymbol{\alpha}_{\mathrm{em}}\\ \boldsymbol{\alpha}_{\mathrm{me}} & \boldsymbol{\alpha}_{\mathrm{mm}}\end{bmatrix}=\begin{bmatrix}\mathbf{P}\\ \mathbf{M}\end{bmatrix}\left(\mathbf{\Sigma}-\mathbf{Z}\right)^{-1}\mathbf{Q}\mathbf{F}^{-1}. \tag{3.7}$$

The only pending issue is to find six suitable excitations generated by incident electric fields $\boldsymbol{E}_i\left(\boldsymbol{r}\right)$. Note, that magnetic fields $\boldsymbol{B}_i\left(\boldsymbol{r}\right)$ cannot be chosen freely as they are connected to the electric fields via free space Maxwell's equations.

3.1. Normalization of the polarizability tensors

As it stands, formula (3.7) is not well suited for an implementation in finite numerical precision. The reason are different units of four polarizability tensors involved and thus a varying number of achievable significant digits. To solve this issue, a suitable removal of units is necessary. As a by-product, one also obtains quantities independent of the absolute dimensions of the scatterer.

For numerical implementation of (3.7) and for presentation of results in Chapter 5 we first transform

$$\begin{aligned} \mathbf{P} &\to \mathrm{c}_0 \frac{\mathbf{P}}{V_0}, \\ \mathbf{M} &\to \frac{\mathbf{M}}{V_0}, \end{aligned} \tag{3.8}$$

where V_0 is defined as

$$V_0 = \frac{4}{3}\pi a^3. \tag{3.9}$$

Second, the feeding matrix $\mathbf{F}$ is transformed according to

$$\boldsymbol{B} \to \mathrm{c}_0 \boldsymbol{B}. \tag{3.10}$$

Third, the loss and impedance matrix are transformed as

$$\boldsymbol{\Sigma} - \mathbf{Z} \to \frac{\boldsymbol{\Sigma} - \mathbf{Z}}{\mathrm{Z}_0}, \tag{3.11}$$

where Z_0 is the impedance of vacuum.

Lastly, the polarizability tensors are transformed as

$$\begin{bmatrix} \boldsymbol{\alpha}_{\mathrm{ee}} & \boldsymbol{\alpha}_{\mathrm{em}} \\ \boldsymbol{\alpha}_{\mathrm{me}} & \boldsymbol{\alpha}_{\mathrm{mm}} \end{bmatrix} \to \frac{1}{V_0} \begin{bmatrix} \varepsilon_0^{-1} \boldsymbol{\alpha}_{\mathrm{ee}} & \mathrm{Z}_0 \boldsymbol{\alpha}_{\mathrm{em}} \\ \mathrm{Z}_0 \boldsymbol{\alpha}_{\mathrm{me}} & \mu_0 \boldsymbol{\alpha}_{\mathrm{mm}} \end{bmatrix}. \tag{3.12}$$

3.2. Feeding

Final step in the calculation of the polarizability tensors is to obtain the excitation matrix **Q** and the feeding matrix **F**. At beginning of Chapter 3 it was mentioned that exactly six linearly independent excitations are needed. Six independent waves produce regular matrix **F**, and only regular matrix has its inverse matrix $\mathbf{F}^{-1}$. This Section introduces two excitation options.

3.2.1. Feeding with plane waves

First option is to use plane waves. Elementary relations for plane waves read

$$\begin{bmatrix} \boldsymbol{E} \\ \mathrm{c}_0 \boldsymbol{B} \end{bmatrix} = \begin{bmatrix} \boldsymbol{E}_0 \\ \boldsymbol{n} \times \boldsymbol{E}_0 \end{bmatrix} \mathrm{e}^{-\mathrm{j}k\boldsymbol{n}\cdot\boldsymbol{r}}, \tag{3.13}$$

where $\boldsymbol{n}$ is a unit vector in the direction of the plane wave propagation and $\boldsymbol{E}_0$ is a vector in the direction of polarization. Here we assume $\boldsymbol{E}_0 = 1\ \mathrm{V}\cdot\mathrm{m}^{-1}$. The direction of electric field is further restricted by

$$\boldsymbol{n}\cdot\boldsymbol{E}_0 = 0. \tag{3.14}$$

As a particular case, we chose waves propagating and being polarized solely along coordinate axes, i.e.

$$\mathbf{F} = \begin{bmatrix} E_x \\ E_y \\ E_z \\ \mathrm{c}_0 B_x \\ \mathrm{c}_0 B_y \\ \mathrm{c}_0 B_z \end{bmatrix} = \begin{bmatrix} 0 & 0 & 1 & 0 & 1 & 0 \\ 1 & 0 & 0 & 0 & 0 & 1 \\ 0 & 1 & 0 & 1 & 0 & 0 \\ 0 & 0 & 0 & h_4 & 0 & h_6 \\ 0 & h_2 & 0 & 0 & h_5 & 0 \\ h_1 & 0 & h_3 & 0 & 0 & 0 \end{bmatrix}, \tag{3.15}$$

where $h_1 - h_6$ are constants with values of plus or minus unity. The columns of (3.15) need to be linearly independent, i.e. we require

$$\det(\mathbf{F}) = (h_2 h_3 h_6 - h_1 h_4 h_5) \neq 0. \tag{3.16}$$

The equation (3.16) has 32 solutions, which read

Table 3-1: Solutions of equation (3.16), part 1

h_1	1	1	1	1	1	1	1	1	1	1	1	1	1	1	1	1
h_2	1	1	1	1	1	1	1	1	−1	−1	−1	−1	−1	−1	−1	−1
h_3	1	1	1	1	−1	−1	−1	−1	1	1	1	1	−1	−1	−1	−1
h_4	1	1	−1	−1	1	1	−1	−1	1	1	−1	−1	1	1	−1	−1
h_5	1	−1	1	−1	1	−1	1	−1	1	−1	1	−1	1	−1	1	−1
h_6	−1	1	1	−1	1	−1	−1	1	1	−1	−1	1	−1	1	1	−1

Table 3-2: Solutions of equation (3.16), part 2

h_1	−1	−1	−1	−1	−1	−1	−1	−1	−1	−1	−1	−1	−1	−1	−1	−1
h_2	1	1	1	1	1	1	1	1	−1	−1	−1	−1	−1	−1	−1	−1
h_3	1	1	1	1	−1	−1	−1	−1	1	1	1	1	−1	−1	−1	−1
h_4	1	1	−1	−1	1	1	−1	−1	1	1	−1	−1	1	1	−1	−1
h_5	1	−1	1	−1	1	−1	1	−1	1	−1	1	−1	1	−1	1	−1
h_6	1	−1	−1	1	−1	1	1	−1	−1	1	1	−1	1	−1	−1	1

Under the assumption of electrical small scatterer, all the above excitations are like and quite arbitrarily, we choose

$$\mathbf{F} = \begin{bmatrix} 0 & 0 & 1 & 0 & 1 & 0 \\ 1 & 0 & 0 & 0 & 0 & 1 \\ 0 & 1 & 0 & 1 & 0 & 0 \\ 0 & 0 & 0 & 1 & 0 & -1 \\ 0 & 1 & 0 & 0 & 1 & 0 \\ 1 & 0 & 1 & 0 & 0 & 0 \end{bmatrix} \tag{3.17}$$

for the later calculations.

Calculation of the excitation matrix **Q** is detailed in Appendix 7.8.

3.2.2. Feeding with Bessel's waves

An interesting possibility would be to have normalized feeding matrix **F** equal to the identity matrix. This can be accomplished by using cylindrical waves as an excitation.

As an example, the incident wave belonging to the third column of **F**, e. g. $\boldsymbol{E}(0)=\mathbf{z}_0$, $\mathrm{c}_0\boldsymbol{B}_0=0$ can be obtained by

$$\boldsymbol{E}=\mathbf{z}_0\,\mathrm{J}_0(k\rho), \tag{3.18}$$

where $\rho=\sqrt{x^2+y^2}$ and J_n is the Bessel's function of the first kind and order *n*.
Faraday's law leads to

$$\mathrm{c}_0\boldsymbol{B}=\mathrm{j}\boldsymbol{\varphi}_0\,\mathrm{J}_1(k\rho). \tag{3.19}$$

Similar procedure leads to the excitation corresponding to the sixth column of the excitation matrix **F**. In this case, one chooses

$$\begin{aligned}\boldsymbol{E}&=-\mathrm{j}\boldsymbol{\varphi}_0\,\mathrm{J}_1(k\rho),\\ \mathrm{c}_0\boldsymbol{B}&=\mathbf{z}_0\mathrm{c}_0\,\mathrm{J}_0(k\rho).\end{aligned} \tag{3.20}$$

The excitation corresponding to other columns of matrix **F** can easily be obtained by rotation of (3.18) – (3.20). Calculation of the excitation matrix **Q** is detailed in Appendix 7.8.

4. Implementation in MATLAB

All necessary expressions have been implemented in MATLAB [18] in a class named "Polarizability". Figure 4-1 shows a working diagram of the class.

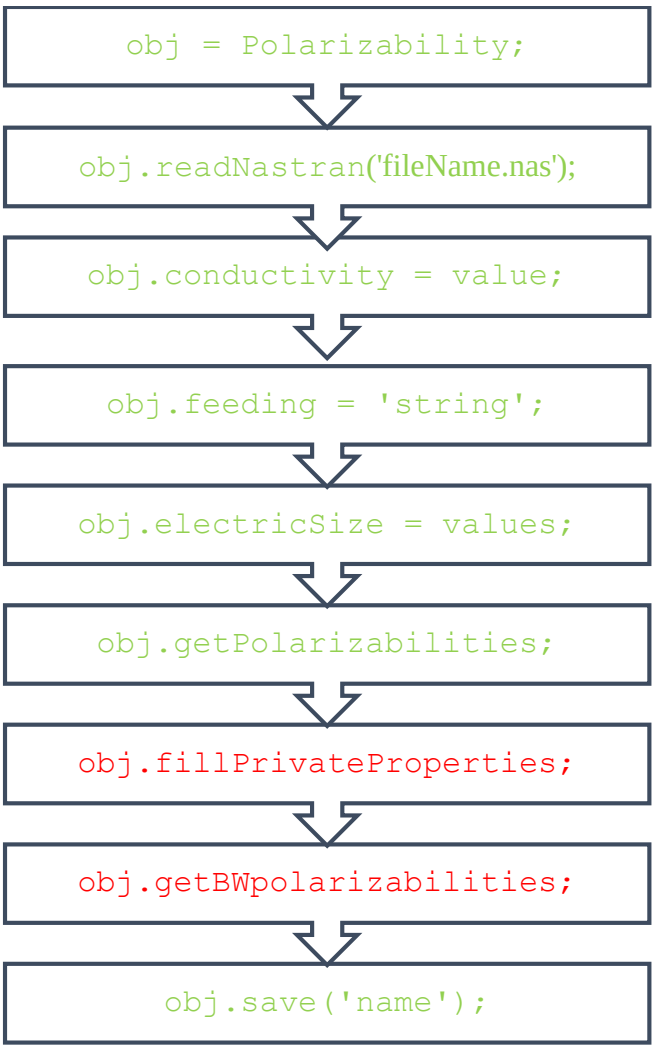

Figure 4-1: Working diagram of the Polarizability class; green colour denotes public commands, red colour denotes private commands

For calculation of polarizability tensors, the user have to first call the constructor of the class

```
obj = Polarizability();
```

Class Polarizability has several required inputs; the main input is a triangular mesh of the studied object. Allowed format is a NASTRAN [19] file. User can easily import data from NASTRAN with command

```
obj.readNastran('nameOfFile.nas');
```

Imported mesh can be shown in a figure

```
obj.plot();
```

Second input is a conductivity of the scatterer. It can easily be set by

```
obj.conductivity = value;
```

The class supports two types of feeding. If user wants to calculate the tensors with plane waves feeding then he sets feeding to 'PW'. If he wants to use Bessel's wave so he sets feeding to 'BW'. If he wants to use both feeding he can use 'PWBW'. The command reads

```
obj.feeding = 'string';
```

The last input is a vector of electric sizes *ka*. The first possibility is to set electric sizes directly with command

```
obj.electricSize = values;
```

The second possible way is to set frequencies of the object by command

```
obj.frequency = values;
```

Property “frequency” is dependent property with setter and getter methods, it depends on “electricSize”, the relation between them is

$$f = \frac{kac_0}{2\pi a}, \tag{4.1}$$

where a is calculated automatically from the supplied triangular mesh.

When all inputs are given in the object then the calculation can start with command

```
obj.getPolarizabilities();
```

In the first step, this method calls method “fillPrivateProperties”. This method calculates matrices **Z**, **Σ**, **P** and **M**. When calculation of private properties is finished, then the calculation of the excitation matrix and polarizability tensors begins. Two methods handle this job, one for plane waves and one for Bessel’s waves. Their names are “getPWpolarizabilities” and “getBWpolarizabilities”.

Polarizability tensors are stored in two structure arrays, the first for plane waves and the second for Bessel’s waves. User can access these variables as

```
struct1 = obj.polBW;
struct2 = obj.polPW;
```

Results can be saved in a .mat file as

```
obj.save('nameOFfile');
```

This command saves both polarizability structure arrays, electric sizes and some additional information about triangular mesh.

Graphical user interface (GUI) was also developed. Print screen of GUI can be seen in Figure 4-2.

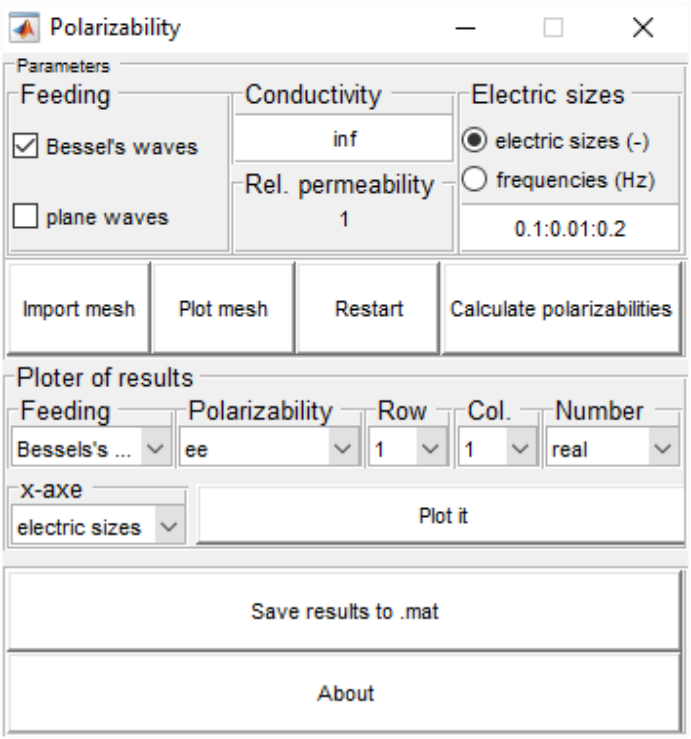

Figure 4-2: GUI of the Polarizability class

5. Results

The code presented in the last Chapter has been used for calculating polarizability of a sphere, a cube and a broadside-coupled split ring resonator (BCSRR) [20]. These shapes were used for verification purposes since their polarizabilities are known analytically, for polarizability of a sphere see [7], for polarizability of a cube see [9] and for polarizability of a BCSRR see [20], [21]. All the results presented in this Chapter are normalized according to (3.12). If we do not state otherwise all object are assumed to be made of perfect electric conductor (PEC).

5.1. Polarizability of a sphere and a cube

Normalized static polarizability matrices for a sphere are analytically given by [7]

$$\boldsymbol{\alpha}_{\mathrm{ee}} = 3\mathbf{U}, \tag{5.1}$$

$$\boldsymbol{\alpha}_{\mathrm{mm}} = -\frac{3}{2}\mathbf{U}, \tag{5.2}$$

where **U** is the identity matrix.

For the numerical evaluation, a PEC sphere of electrical size $ka = 0.01$ was discretized into 1504 triangles (see Figure 5-1) and its polarizabilities have been evaluated (with Bessel's feeding) via the code described in Chapter 4. The results are:

$$\boldsymbol{\alpha}_{\mathrm{ee}} \approx 3.0157\mathbf{U}, \tag{5.3}$$

$$\boldsymbol{\alpha}_{\mathrm{mm}} \approx -1.5072\mathbf{U}. \tag{5.4}$$

To the best of author's knowledge, an analytical formula for the polarizability of a cube does not exist. There however exist very precise numerical evaluation of its static polarizability [9], [10]

$$\boldsymbol{\alpha}_{\mathrm{ee}} \approx 1.3394\mathbf{U}, \tag{5.5}$$

$$\boldsymbol{\alpha}_{\mathrm{mm}} \approx -0.6022\mathbf{U}. \tag{5.6}$$

For a numerical evaluation, PEC cube of electrical size $ka = 0.01$ was discretised into 1584 triangles (see Figure 5-1) and its polarizabilities have been evaluated (with Bessel's feeding) via the code described in Chapter 4. The results are:

$$\boldsymbol{\alpha}_{\mathrm{ee}} \approx 1.3520\mathbf{U}, \tag{5.7}$$

$$\boldsymbol{\alpha}_{\mathrm{mm}} \approx -0.6095\mathbf{U}. \tag{5.8}$$

Excellent agreement with analytical result can be observed in both aforementioned cases.

5.2. Radiation resistance

Figure 5-1 presents the numerical polarizability extraction for a given frequency sweep. It can be seen that results are very close to the known static values for small electric sizes. The small discrepancies can be attributed to meshing. Differences grow with increasing *ka*, the reason being the radiation resistance of the scatterer. In this case, the results obtained via the method of this thesis should be considered as correct ones, since the analytical formulas for polarizabilities are strictly valid only at $ka = 0$ and are not supposed to be precise at $ka > 0$.

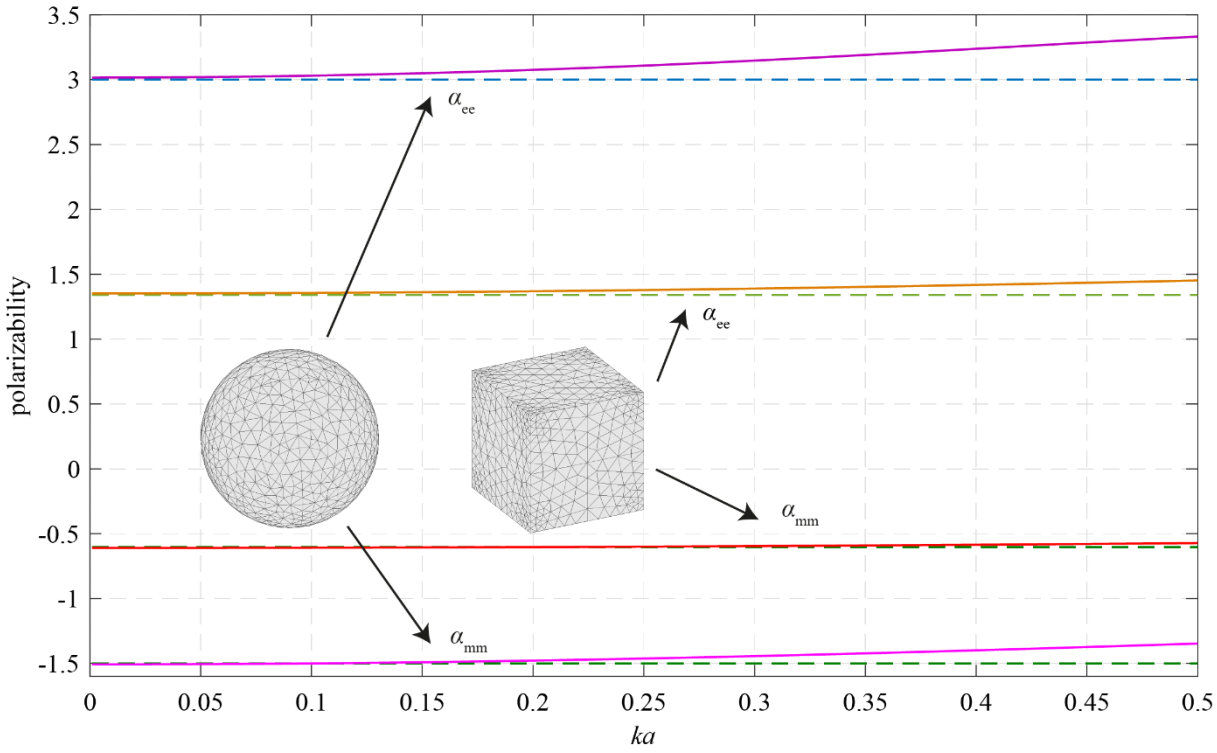

Figure 5-1: The real part of the normalized electric and magnetic polarizability of a PEC sphere and a PEC cube obtained by the method proposed in this thesis (Bessel's waves feeding, solid lines). The results are compared to their known static values (dashed lines).

5.3. The accuracy of the method for $ka \to 0$

When the electrical size approaches zero, the dynamical formulation of the presented method brings unpleasant numerical issues. First problem comes from a frequency dependence of the impedance matrix $\mathbf{Z}$ (see Section 7.6), which becomes ill-defined at $ka \to 0$. Second possible issue relates to the Bessel's feeding. In that case the sole excitation by magnetic field at $ka \to 0$ in fact produces no excitation at all in the EFIE formulation (3.7). These two problems were explored and results can be seen in Figure 5-2 for both, the Bessel's wave and plane wave feeding. It can be seen that for *ka* smaller than 10^{-6}, the used double precision numerics breaks down, producing meaningless results. This numerical problem comes from the impedance matrix and it is common to both excitations types. As a result, the Bessel's feeding brings no practical issues in the *ka* ranges allowed by the impedance matrix and it can be safely used for calculating the polarizability tensors.

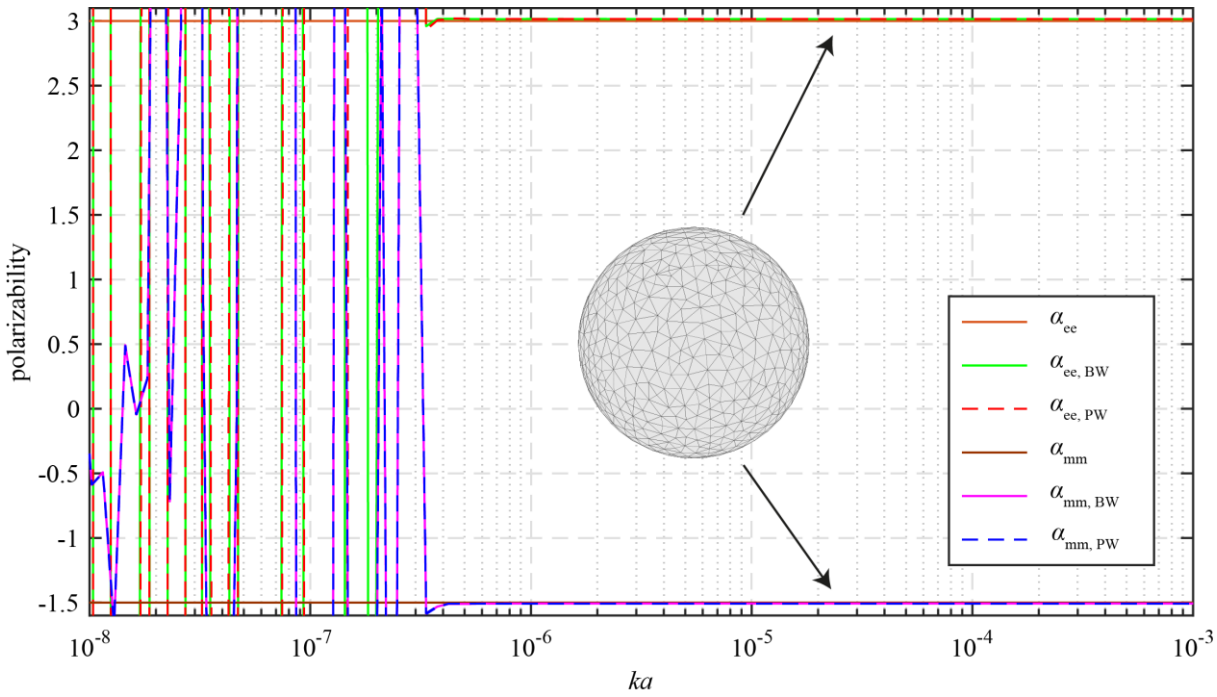

Figure 5-2: The real part of the normalized electric and magnetic polarizability of a PEC sphere. Two different excitations of the dynamical extraction method are used, see Section 3.2. The results are compared to their known static values.

5.4. BCSRR

Encouraged by the good performance of the method on canonical objects, we can try to test it in more complicated scenario, when radiation effects become important. In that respect, the PEC resonant scatterers of non-negligible electrical sizes are interesting testing grounds. As one example, we have chosen the BCSRR [20], extensively used in the design of magnetic metamaterials [22]. The geometry of the scatterer is illustrated in Figure 5-3. Formula for the magnetic polarizability tensor, which is presented in [20], [21] and is used for comparison with numerical results, reads

$$\alpha_{\mathrm{mm}}^{zz} = \frac{\pi^2}{L}\left(r_{\mathrm{ext}} - \frac{w}{2}\right)^4 \left(\frac{\omega_0^2}{\omega^2} - 1 + \mathrm{j}\frac{R_{\mathrm{rad}}}{\omega L}\right)^{-1} \frac{\mu_0}{V_0}, \tag{5.9}$$

where r_{ext} is an external radius of the ring, w is the width of the strip, L is the self-inductance [21], ω_0 is the angular frequency at resonance, μ_0 is the permeability of vacuum and

$$R_{\mathrm{rad}} = \frac{Z_0 \pi k^4}{6}\left(r_{\mathrm{ext}} - \frac{w}{2}\right)^4, \tag{5.10}$$

represents the radiation losses [8], [23]. An excellent agreement can be observed between analytical model and results from the method of this thesis.

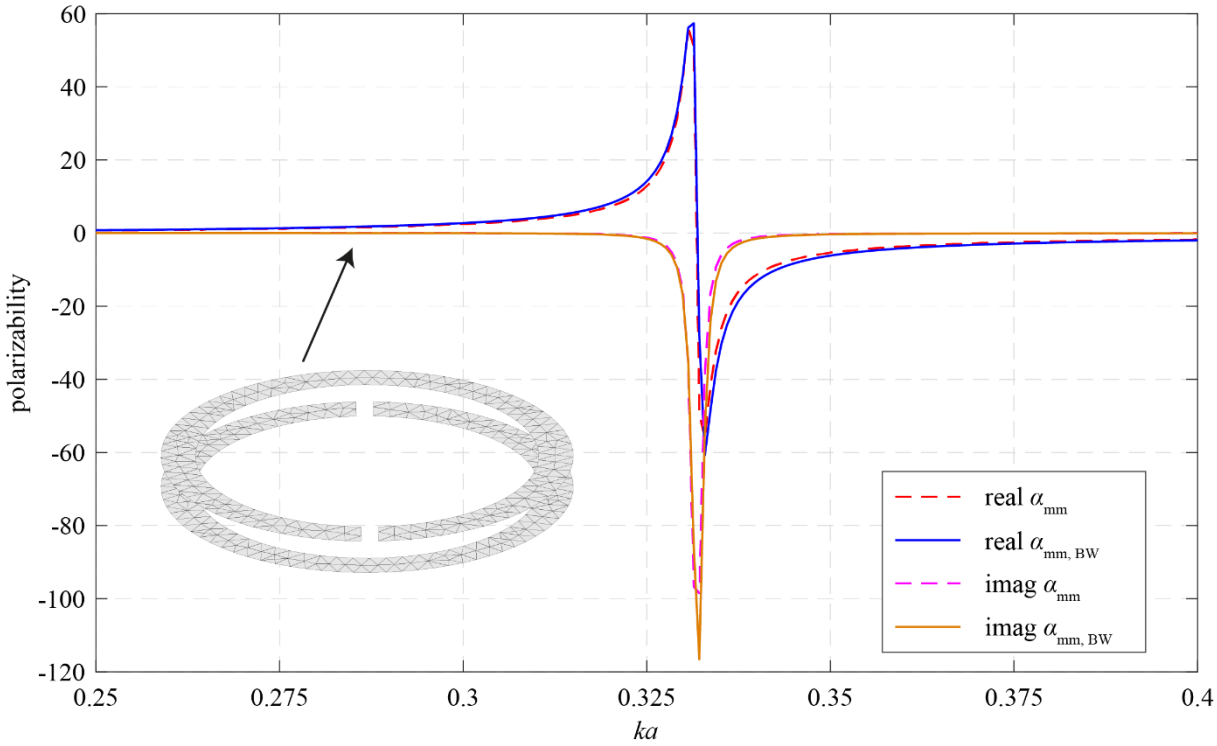

Figure 5-3: The real and imaginary part of the normalized magnetic polarizability of the BCSRR made of PEC. The results are compared to analytical model (dashed lines). Results obtained by the method proposed in this thesis are presented as solid lines.

The BCSSR can also be used to test the presence of the ohmic losses. In this case, the analytical model (5.9) can easily be extended with $R_{\text{rad}} \to R_{\text{rad}} + R_{\text{loss}}$, where

$$R_{\text{loss}} = \frac{2\pi}{w\sigma\delta}\left(r_{\text{ext}} - \frac{w}{2}\right) \tag{5.11}$$

represents the conduction losses [21], with σ as conductivity of the used material and $\delta = \sqrt{2/(\omega\sigma\mu_0)}$ as the penetration depth. The results from the analytically model and from the numerical extraction are compared in Figure 5-4. In order to keep the problem scalable, the ratio $\sigma/(\omega\varepsilon_0)$ has been fixed at 10^7. Again, very good agreement can be observed.

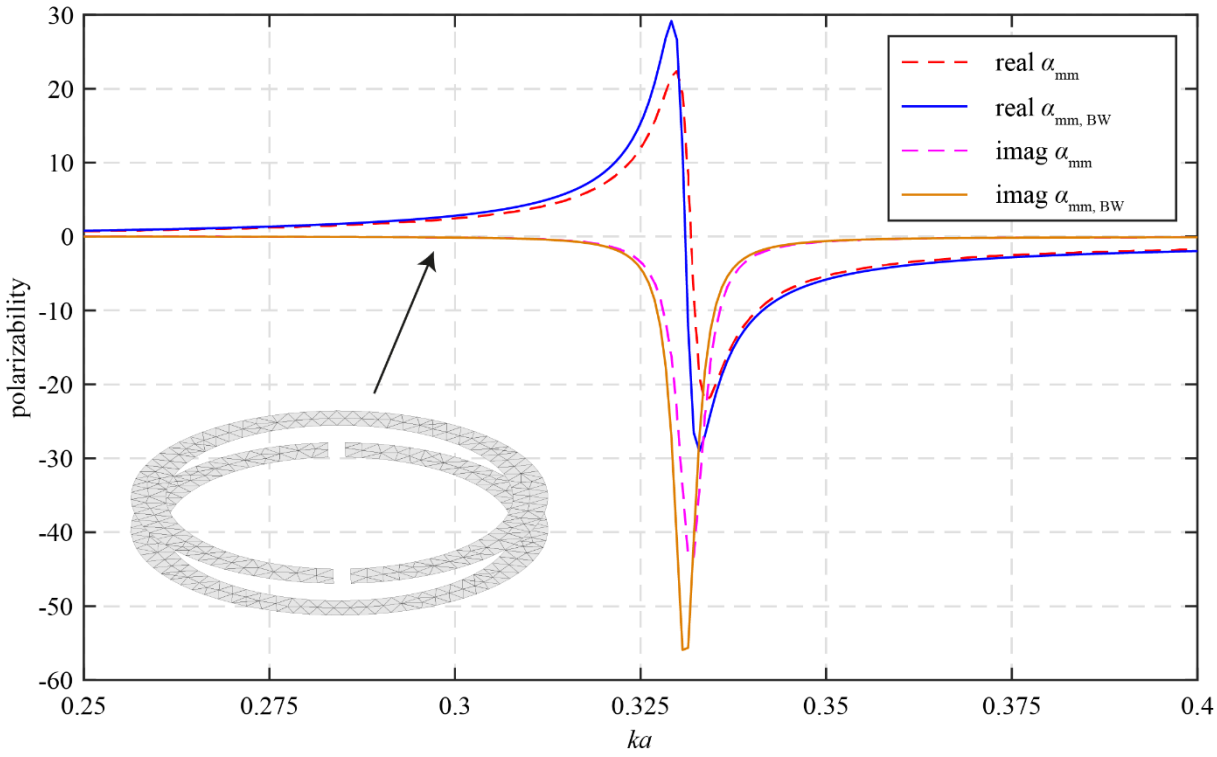

Figure 5-4: The real and imaginary part of the normalized magnetic polarizability of the lossy BCSRR. The results are compared to analytical model (dashed lines). Results obtained by the method proposed in this thesis are presented as solid lines.

6. Conclusion

We have become acquainted with the definition of polarizability tensors and derived relations for their extraction for an arbitrarily shaped electrically small scatterer. The relations have been implemented in MATLAB and the codes have been used for calculation polarizability tensors of electric small objects as a sphere, a cube and a BCSRR. These objects were chosen for their known polarizability tensors. Excellent agreement between our numerical results and analytically models has been observed in static and dynamic ranges. The implemented numerical method have important advantage of considering radiation and ohmic losses.

All codes, which were programmed for the thesis, are freely available on CD, which is attached to the diploma thesis and can be found on MATLAB file exchange, the link is http://goo.gl/LVWTjc. This fast and effective evaluation of polarizability tensors invites for various optimization tasks concerning electrically small scatterers, which purpose can be found in the design of artificial media, radio identification tags and beam-forming arrays.

7. Appendices

7.1. Electric field integral equation

The continuous form of the electric field integral equation (EFIE) [17] used throughout this thesis reads

$$Z_S \boldsymbol{K}(\boldsymbol{r}) = \boldsymbol{E}(\boldsymbol{r}) + k^2 L\{\boldsymbol{K}(\boldsymbol{r})\} + \nabla L\{\nabla \cdot \boldsymbol{K}(\boldsymbol{r})\}, \tag{7.1}$$

with $\boldsymbol{K}(\boldsymbol{r})$ being the surface current density induced on the scatterer, $\boldsymbol{E}(\boldsymbol{r})$ being the incident electric field and with operator L defined as

$$L\{\boldsymbol{F}(\boldsymbol{r}')\} = \frac{-\mathrm{j}}{4\pi\omega\varepsilon} \int_{S'} \boldsymbol{F}(\boldsymbol{r}') \frac{\mathrm{e}^{-\mathrm{j}k|\boldsymbol{r}-\boldsymbol{r}'|}}{|\boldsymbol{r}-\boldsymbol{r}'|} \mathrm{d}S'. \tag{7.2}$$

The quantity $Z_S = (1+\mathrm{j})/(\sigma\delta)$ represents the surface impedance of the conducting half-space [1] with $\delta = \sqrt{2/(\omega\mu\sigma)}$ being the penetration depth (we consider only non-magnetic materials, thus $\mu = \mu_0$.). The left side of (7.1) thus approximates the reaction of a lossy conductor in the cases when the penetration depth is negligible with respect to the thickness and with respect to the curvature radius of any part of the scatterer. Utilizing expansion

$$\boldsymbol{K}(\boldsymbol{r}) = \sum_n I_n \boldsymbol{f}_n(\boldsymbol{r}), \tag{7.3}$$

the integral equation (7.1) is recast into its matrix form [24]

$$(\boldsymbol{\Sigma} - \mathbf{Z})\mathbf{I} = \begin{bmatrix} \langle \boldsymbol{f}_1, \boldsymbol{E} \rangle \\ \vdots \\ \langle \boldsymbol{f}_N, \boldsymbol{E} \rangle \end{bmatrix}, \tag{7.4}$$

where

$$\mathbf{Z} = \left[k^2 \langle \boldsymbol{f}_m, L\{\boldsymbol{f}_n\} \rangle - \langle \nabla \cdot \boldsymbol{f}_m, L\{\nabla \cdot \boldsymbol{f}_n\} \rangle \right] \tag{7.5}$$

is the so-called impedance matrix [17], [24] and where

$$\mathbf{\Sigma} = Z_S \left[\left\langle \boldsymbol{f}_m, \boldsymbol{f}_n \right\rangle \right] \tag{7.6}$$

is the matrix representing the reaction of a lossy conductor.

7.2. Triangular mesh

Proposed numerical method for extraction of polarizability tensors needs suitable basis functions $\boldsymbol{f}_n(\boldsymbol{r})$ and a suitable discretization of the scatterer. This Section introduces the triangular mesh and the Rao-Wilton-Glisson basis, which are used in the thesis.

7.2.1. Process of triangulation and triangular mesh

Triangulation [25] is a process, which discretizes smooth surface Ω to a finite number of triangles T_n which are able to represent the original structure in computer's memory. The process can mathematically be described as

$$\begin{aligned} &\Omega \to \mathcal{D}(\Omega, N) \to T_n, \\ &T_i \cap T_j = \varnothing, i \neq j, \\ &T_i \cap T_j = T_i, i = j, \\ &\bigcup_{n=1}^{N} T_n = \Omega, \end{aligned} \tag{7.7}$$

in which $\mathcal{D}$ denotes the discretization scheme and N is the number of triangles T.

Triangular mesh is commonly defined by two matrices $\mathbf{p}^{[M\times 3]}$ and $\mathbf{t}^{[N\times 3]}$. Matrix $\mathbf{p}^{[M\times 3]}$ consists of radius vectors of all M mesh points. Matrix $\mathbf{t}^{[N\times 3]}$ gives information on which three nodes from **p** form a triangle.

7.2.2. Pair of triangles, Rao-Wilton-Glisson basis

Triangulation gave us a triangular mesh. We then use pairs of triangles with common edges and define Rao-Wilton-Glisson (RWG) function [15], see Figure 7-1, as

$$\boldsymbol{f}_n(\boldsymbol{r}) = \begin{cases} \dfrac{l_n}{2A_n^+}\boldsymbol{\rho}_n^+, \boldsymbol{r} \in T_n^+ \\ \dfrac{l_n}{2A_n^-}\boldsymbol{\rho}_n^-, \boldsymbol{r} \in T_n^- \\ 0, \text{otherwise}, \end{cases} \tag{7.8}$$

where l_n, $A_n^{\pm}$ denote the edge length and area of triangle, respectively. Vectors $\boldsymbol{\rho}_n^{\pm}$ are defined as

$$\begin{aligned} \boldsymbol{\rho}_n^+ &= \boldsymbol{r} - \mathbf{V}_{1,n}, \\ \boldsymbol{\rho}_n^- &= \mathbf{V}_{4,n} - \boldsymbol{r}, \end{aligned} \tag{7.9}$$

where $\mathbf{V}_1$ and $\mathbf{V}_4$ are free vertices according to Figure 7-1. The triangle containing $\mathbf{V}_1$ is denoted as positive, while the triangle containing $\mathbf{V}_4$ as negative. The expansion coefficients I_n, see (7.3), represents surface current density flowing normally to the common edge defined by vertices $\mathbf{V}_2$ and $\mathbf{V}_3$.

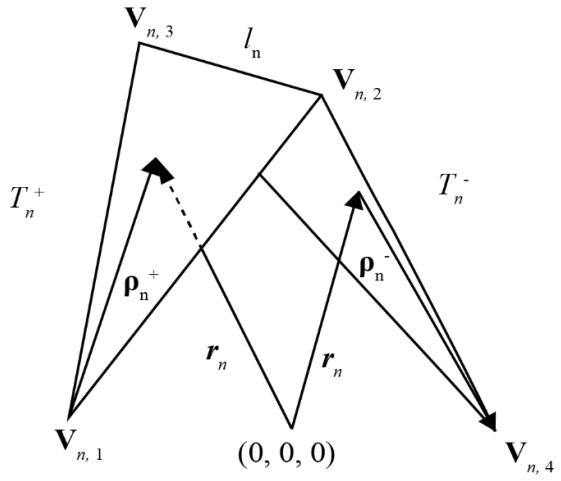

Figure 7-1: Forming RWG function

Majority of triangles are shared between three or more RWG functions, only boundary triangles are shared between two or only one RWG function. This property gives the RWG basis great flexibility for describing surface current density $\boldsymbol{K}(\boldsymbol{r})$ in the form (7.3).

7.3. Barycentric coordinate system

Barycentric coordinate system [26] can help us with solving integrals over arbitrary triangle, which become very handy in dealing with the RWG basis. Barycentric coordinates α, β, γ are defined by three vertices $\mathbf{V}_1$, $\mathbf{V}_2$, $\mathbf{V}_3$ and transformation

$$\boldsymbol{r} = \begin{pmatrix} x \\ y \\ z \end{pmatrix} = \mathbf{T} \begin{pmatrix} \gamma \\ \alpha \\ \beta \end{pmatrix}. \tag{7.10}$$

$$\mathbf{T} = \begin{pmatrix} x_1 & x_2 & x_3 \\ y_1 & y_2 & y_3 \\ z_1 & z_2 & z_3 \end{pmatrix}, \tag{7.11}$$

where columns of the matrix $\mathbf{T}$ are the Cartesians coordinates of vertices $\mathbf{V}_1$, $\mathbf{V}_2$, $\mathbf{V}_3$. Important attribute of the barycentric coordinates is their normalization

$$1 = \gamma + \alpha + \beta. \tag{7.12}$$

The graphical representation of the barycentric coordinates is depicted in Figure 7-2 and shows how an arbitrary triangle is transform into a rectangular isosceles triangle.

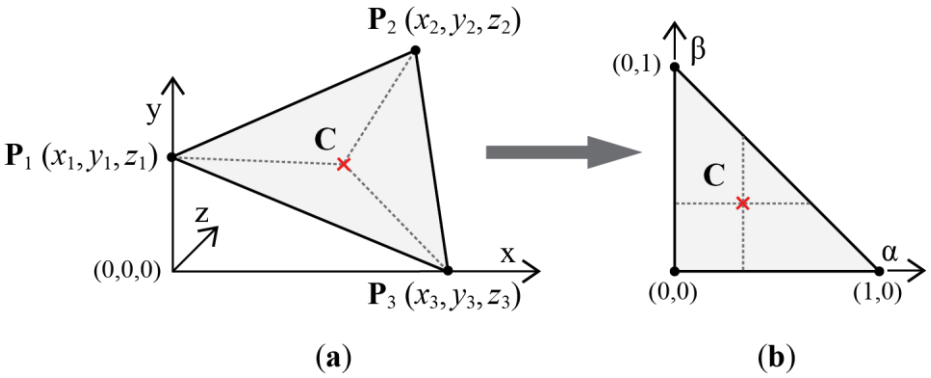

Figure 7-2: Barycentric coordinate system

Transformation (7.10) together with (7.12) allows then to write an integration of an arbitrary function over a given triangle as

$$\int_T f(\boldsymbol{r})\,\mathrm{d}\boldsymbol{r} = 2A\int_0^1\int_0^{1-\beta} f\left(\alpha\mathbf{V}_1+\beta\mathbf{V}_2+(1-\alpha-\beta)\mathbf{V}_3\right)\mathrm{d}\alpha\,\mathrm{d}\beta, \tag{7.13}$$

where A is area of the triangle and $2A$ is the Jacobian. This result follows from the fact that a rectangle in barycentric coordinates corresponds to a quadrilateral in Cartesian coordinates, and the ratio of the areas of the corresponding shapes in the corresponding coordinate systems is given by $2A$.

7.4. Derivation of matrix P in RWG basis

The substitution of (3.3), (7.8) into (2.2) leads to

$$\boldsymbol{p} = \frac{1}{\mathrm{j}\omega}\int_S \boldsymbol{K}(\boldsymbol{r})\,\mathrm{d}S = \frac{1}{\mathrm{j}\omega}\sum_n I_n\left(\int_s \boldsymbol{f}_n(\boldsymbol{r})\,\mathrm{d}S\right) = \frac{1}{\mathrm{j}\omega}\sum_n I_n\left(\frac{l_n}{2A_n^+}\int_{\Delta_n^+}\boldsymbol{\rho}_n^+\,\mathrm{d}S + \frac{l_n}{2A_n^-}\int_{\Delta_n^-}\boldsymbol{\rho}_n^-\,\mathrm{d}S\right). \tag{7.14}$$

Equation (7.14) can be rewritten into the matrix form

$$\begin{aligned}
&\mathbf{p} = \mathbf{P}\mathbf{I},\\
&\mathbf{P}_n = \mathbf{P}_n^+ + \mathbf{P}_n^-,\\
&\mathbf{P}_n^+ = \frac{l_n}{\mathrm{j}2A_n^+\omega}\int_{\Delta_n^+}\boldsymbol{\rho}_n^+\,\mathrm{d}S,\\
&\mathbf{P}_n^- = \frac{l_n}{\mathrm{j}2A_n^-\omega}\int_{\Delta_n^-}\boldsymbol{\rho}_n^-\,\mathrm{d}S,
\end{aligned} \tag{7.15}$$

where $\mathbf{P}_n^{[3\times1]}I_n^{[1\times1]}$ corresponds to the electric dipole moment of the *n*-th RWG function.

The integral describing $\mathbf{P}_n^+$ is evaluated as follows

$$\mathbf{P}_n^+ = \frac{l_n}{\mathrm{j}2A_n^+\omega}\int_{\Delta_n^+}\boldsymbol{\rho}_n^+\,\mathrm{d}S = \frac{l_n}{\mathrm{j}2A_n^+\omega}\int_{\Delta_n^+}\left(\boldsymbol{r}-\mathbf{V}_{1,n}\right)\mathrm{d}S = \frac{l_n}{\mathrm{j}2A_n^+\omega}\left(\mathbf{x_0}\int_{\Delta_n^+}\left(x-x_{1,n}\right)\mathrm{d}S + \mathbf{y_0}\int_{\Delta_n^+}\left(y-y_{1,n}\right)\mathrm{d}S + \mathbf{z_0}\int_{\Delta_n^+}\left(z-z_{1,n}\right)\mathrm{d}S\right). \tag{7.16}$$

Transforming triangle T_n^+ to the barycentric coordinate system (see Section 7.3), gives

$$\begin{aligned}
\mathbf{P}_{n,\,\mathrm{x}}^{+} &= \mathbf{x}_0 \frac{l_n}{\mathrm{j}2A_n^{+}\omega} \int_{\Delta_n^{+}} \left(x - x_{1,n}\right) \mathrm{d}S = \\
&\mathbf{x}_0 \frac{l_n}{\mathrm{j}2A_n^{+}\omega} 2A_n^{+} \int_0^1 \int_0^{1-\alpha} \left(x(\alpha,\beta) - x_{1,n}\right) \mathrm{d}\beta\, \mathrm{d}\alpha = \\
&= \mathbf{x}_0 \frac{l_n}{\mathrm{j}\omega} \left(\frac{x_{2,n}}{6} - \frac{x_{1,n}}{3} + \frac{x_{3,n}}{6} \right).
\end{aligned} \tag{7.17}$$

Integrations for *y* and *z* directions are similar, thus

$$\mathbf{P}_n^{+} = \mathbf{P}_{n,\,\mathrm{x}}^{+} + \mathbf{P}_{n,\,\mathrm{y}}^{+} + \mathbf{P}_{n,\,\mathrm{z}}^{+} = \frac{l_n}{\mathrm{j}6\omega} \begin{pmatrix} x_{2,n} + x_{3,n} - 2x_{1,n} \\ y_{2,n} + y_{3,n} - 2y_{1,n} \\ z_{2,n} + z_{3,n} - 2z_{1,n} \end{pmatrix}. \tag{7.18}$$

The result for $\mathbf{P}_n^{+}$ in (7.18) also corresponds to

$$\mathbf{P}_n^{+} = \frac{l_n}{\mathrm{j}2\omega} \boldsymbol{\rho}_n^{+}\left(\mathbf{C}_n^{+}\right) = \frac{l_n}{\mathrm{j}2\omega}\left(\mathbf{C}_n^{+} - \mathbf{V}_{1,n}\right), \tag{7.19}$$

where $\mathbf{C}_n^{+}$ is the centre of the positive triangle

$$\mathbf{C}_n^{+} = \frac{\mathbf{V}_{1,n} + \mathbf{V}_{2,n} + \mathbf{V}_{3,n}}{3}. \tag{7.20}$$

An analogous procedure gives

$$\mathbf{P}_n^{-} = \frac{l_n}{\mathrm{j}2\omega} \boldsymbol{\rho}_n^{-}\left(\mathbf{C}_n^{-}\right) = \frac{l_n}{\mathrm{j}2\omega}\left(\mathbf{V}_{4,n} - \mathbf{C}_n^{-}\right), \tag{7.21}$$

where $\mathbf{C}_n^{-}$ is the centre of the negative triangle

$$\mathbf{C}_n^{-} = \frac{\mathbf{V}_{2,n} + \mathbf{V}_{3,n} + \mathbf{V}_{4,n}}{3}. \tag{7.22}$$

Putting all together,

$$\mathbf{P}_n = \mathbf{P}_n^+ + \mathbf{P}_n^- = \frac{l_n}{\mathrm{j}2\omega}\left(\mathbf{C}_n^+ - \mathbf{V}_{1,n} + \mathbf{V}_{4,n} - \mathbf{C}_n^-\right). \tag{7.23}$$

Now we use (7.20), (7.22) and write

$$\mathbf{P}_n = \frac{l_n}{\mathrm{j}\omega}\left(\mathbf{C}_n^+ - \mathbf{C}_n^-\right). \tag{7.24}$$

7.5. Derivation of matrix M in RWG basis

The substitution of (3.3), (7.8) into (2.3)

$$\begin{aligned} \boldsymbol{m} = \frac{1}{2}\int_S \left(\boldsymbol{r}\times\boldsymbol{K}\left(\boldsymbol{r}\right)\right)\mathrm{d}S = \sum_n I_n\left(\int_s \left(\boldsymbol{r}\times\boldsymbol{f}_n(\boldsymbol{r})\right)\,\mathrm{d}S\right) = \\ \frac{1}{2}\sum_n I_n\left(\frac{l_n}{2A_n^+}\int_{\Delta_n^+}\left(\boldsymbol{r}\times\boldsymbol{\rho}_n^+\right)\mathrm{d}S + \frac{l_n}{2A_n^-}\int_{\Delta_n^-}\left(\boldsymbol{r}\times\boldsymbol{\rho}_n^-\right)\mathrm{d}S\right). \end{aligned} \tag{7.25}$$

Equation (7.25) can be rewritten into the matrix form

$$\begin{aligned} &\boldsymbol{m} = \mathbf{M}\mathbf{I}, \\ &\mathbf{M} = \mathbf{M}^+ + \mathbf{M}^-, \\ &\mathbf{M}_n^+ = \frac{l_n}{4A_n^+}\int_{\Delta_n^+}\left(\boldsymbol{r}\times\boldsymbol{\rho}_n^+\right)\mathrm{d}S, \\ &\mathbf{M}_n^- = \frac{l_n}{4A_n^-}\int_{\Delta_n^-}\left(\boldsymbol{r}\times\boldsymbol{\rho}_n^-\right)\mathrm{d}S, \end{aligned} \tag{7.26}$$

where $\mathbf{M}_n^{[3\times1]}I_n^{[1\times1]}$ corresponds to the magnetic dipole moment of the *n*-th RWG function.

The integral describing $\mathbf{M}_n^+$ is evaluated as follows

$$\begin{aligned}
&\mathbf{M}_n^+ = \frac{l_n}{4A_n^+}\int\limits_{\Delta_n^+}\left(\boldsymbol{r}\times\boldsymbol{\rho}_n^+\right)\mathrm{d}S = \\
&\frac{l_n}{4A_n^+}\int\limits_{\Delta_n^+}\left(\boldsymbol{r}\times\left(\boldsymbol{r}-\mathbf{V}_{1,n}\right)\right)\mathrm{d}S = \frac{l_n}{4A_n^+}\int\limits_{\Delta_n^+}\left(\mathbf{V}_{1,n}\times\boldsymbol{r}\right)\mathrm{d}S = \\
&\frac{l_n}{4A_n^+}\int\limits_{\Delta_n^+}\left(\mathbf{V}_{1,n}\times\boldsymbol{r}\right)\mathrm{d}S = \frac{l_n}{4A_n^+}\left(\mathbf{x_0}\int\limits_{\Delta_n^+}\left(y_{1,n}z-z_{1,n}y\right)\mathrm{d}S + \right. \\
&\left.\mathbf{y_0}\int\limits_{\Delta_n^+}\left(z_{1,n}x-x_{1,n}z\right)\mathrm{d}S + \mathbf{z_0}\int\limits_{\Delta_n^+}\left(x_{1,n}y-y_{1,n}x\right)\mathrm{d}S\right).
\end{aligned} \tag{7.27}$$

Transforming triangle T_n^+ to the barycentric coordinate system (see Section 7.3), gives

$$\begin{aligned}
&\mathbf{M}_{n,\mathrm{x}}^+ = \mathbf{x}_0\frac{l_n}{4A_n^+}\int\limits_{\Delta_n^+}\left(y_{1,\mathrm{n}}z-z_{1,\mathrm{n}}y\right)\mathrm{d}S = \\
&\mathbf{x}_0\frac{l_n}{4A_n^+}2A_n^+\int\limits_0^1\int\limits_0^{1-\alpha}\left(y_{1,\mathrm{n}}z(\alpha,\beta)-z_{1,\mathrm{n}}y(\alpha,\beta)\right)\mathrm{d}\beta\,\mathrm{d}\alpha = \\
&= \mathbf{x}_0\frac{l_n}{4}\frac{1}{3}\left(y_{1,\mathrm{n}}\left(z_{2,\mathrm{n}}+z_{3,\mathrm{n}}\right)-z_{1,\mathrm{n}}\left(y_{2,\mathrm{n}}+y_{3,\mathrm{n}}\right)\right).
\end{aligned} \tag{7.28}$$

Integrations for *y* and *z* directions are similar thus,

$$\mathbf{M}_n^+ = \mathbf{M}_{n,\mathrm{x}}^+ + \mathbf{M}_{n,\mathrm{y}}^+ + \mathbf{M}_{n,\mathrm{z}}^+ = \frac{l_n}{12}\begin{pmatrix} y_{1,n}z_{2,n}-z_{1,n}y_{2,n}+y_{1,n}z_{3,n}-z_{1,n}y_{3,n} \\ z_{1,n}x_{2,n}-x_{1,n}z_{2,n}+x_{1,n}z_{3,n}-z_{1,n}x_{3,n} \\ x_{1,n}y_{2,n}-y_{1,n}x_{2,n}+x_{1,n}y_{3,n}-y_{1,n}x_{3,n}\end{pmatrix}. \tag{7.29}$$

The result for $\mathbf{M}_n^+$ in (7.29) also corresponds to (see (7.20))

$$\mathbf{M}_n^+ = \frac{l_n}{4}\left(\mathbf{V}_{1,n}\times\mathbf{C}_n^+\right). \tag{7.30}$$

An analogous procedure gives

$$\mathbf{M}_n^- = \frac{l_n}{4}\left(-\mathbf{V}_{4,n}\times\mathbf{C}_n^-\right). \tag{7.31}$$

Putting all together,

$$\mathbf{M}_n = \mathbf{M}_n^+ + \mathbf{M}_n^- = \frac{l_n}{4}\left(\mathbf{V}_{1,n} \times \mathbf{C}_n^+ - \mathbf{V}_{4,n} \times \mathbf{C}_n^-\right). \tag{7.32}$$

7.6. Impedance matrix $\mathbf{Z}$ in RWG basis

Impedance matrix **Z** determines electromagnetic interaction between different RWG basis functions and depends on a geometry Ω and frequency. The size of the impedance matrix is equal to the number of RWG basis function.

Effective ways of evaluating the matrix terms in (7.5) have been proposed by many authors. We utilize the scheme of Makarov [27], which applies to the RWG basis [15].

7.7. Conduction matrix $\mathbf{\Sigma}$ in RWG basis

In the first step is to show the evaluation of the scalar product (7.6) within the RWG basis for off-diagonal terms. Figure 7-3 shows four cases, which are formally different. Figure 7-3 b was chosen to demonstrate the derivation, thus

$$\begin{aligned} \left\langle \boldsymbol{f}_m, \boldsymbol{f}_n \right\rangle &= \frac{l_m l_n}{4A_m^+ A_n^+} \int_{\Delta_n^+} \left(\boldsymbol{\rho}_m^+ \cdot \boldsymbol{\rho}_n^+\right) \mathrm{d}S = \\ &\frac{l_m l_n}{4A_m^+ A_n^+} \int_{\Delta_n^+} \left(\left(\boldsymbol{r} - \mathbf{V}_{1,m}\right) \cdot \left(\boldsymbol{r} - \mathbf{V}_{1,n}\right)\right) \mathrm{d}S. \end{aligned} \tag{7.33}$$

Transforming triangle T_n^+ to the barycentric coordinate system (see Section 7.3), gives

$$\left\langle \boldsymbol{f}_m, \boldsymbol{f}_n \right\rangle = \frac{l_m l_n}{2A_m^+} \int_0^1 \int_0^{1-\alpha} \left(\left(\boldsymbol{r}(\alpha,\beta) - \mathbf{V}_{1,m}\right) \cdot \left(\boldsymbol{r}(\alpha,\beta) - \mathbf{V}_{1,n}\right)\right) \mathrm{d}\beta \, \mathrm{d}\alpha. \tag{7.34}$$

The solution of (7.34) is lengthy but straightforward and corresponds to

$$\left\langle \boldsymbol{f}_m, \boldsymbol{f}_n \right\rangle = \frac{\chi_{mn} l_m l_n}{24 A_m} \left(9\mathbf{C}_m \cdot \left(\mathbf{C}_m - \mathbf{V}_{f,m} - \mathbf{V}_{f,n} \right) + \left| \mathbf{V}_{f,m} + \mathbf{V}_{f,n} \right|^2 + 5\mathbf{V}_{f,m} \cdot \mathbf{V}_{f,n} \right), \tag{7.35}$$

where index *f* denotes free vertices (the vertices $\mathbf{V}_1$ and $\mathbf{V}_4$) belonging to the triangle common to the *m*-th and the *n*-th RWG function. The coefficient χ_{mn} is equal to one for cases depicted in Figure 7-3 b, c, to minus one for cases depicted in Figure 7-3 d, e and to zero for RWG functions with no common triangle.

The evaluation of the scalar products (7.6) within the RWG basis for diagonal terms, read

$$\left\langle \boldsymbol{f}_m, \boldsymbol{f}_m \right\rangle = \frac{l_m^2}{4\left(A_m^+\right)^2} \int_{\Delta_n^+} \left(\boldsymbol{\rho}_m^+ \cdot \boldsymbol{\rho}_m^+ \right) \mathrm{d}S + \frac{l_m^2}{4\left(A_m^-\right)^2} \int_{\Delta_n^-} \left(\boldsymbol{\rho}_m^- \cdot \boldsymbol{\rho}_m^- \right) \mathrm{d}S. \tag{7.36}$$

The integral over the positive triangle is transformed to the barycentric coordinate system (see Section 7.3), read

$$\begin{aligned} \psi_n^+ &= \frac{l_m^2}{4\left(A_m^+\right)^2} \int_{\Delta_n^+} \left(\boldsymbol{\rho}_m^+ \cdot \boldsymbol{\rho}_m^+ \right) \mathrm{d}S = \frac{l_m^2}{4\left(A_m^+\right)^2} \int_{\Delta_n^+} \left(\left(\boldsymbol{r} - \mathbf{V}_{1,m} \right) \cdot \left(\boldsymbol{r} - \mathbf{V}_{1,m} \right) \right) \mathrm{d}S = \\ &\frac{l_m^2}{2A_m^+} \int_0^1 \int_0^{1-\alpha} \left(\left(\boldsymbol{r}(\alpha,\beta) - \mathbf{V}_{1,m} \right) \cdot \left(\boldsymbol{r}(\alpha,\beta) - \mathbf{V}_{1,m} \right) \right) \mathrm{d}\beta \, \mathrm{d}\alpha. \end{aligned} \tag{7.37}$$

The solution of (7.37) is lengthy but straightforward and corresponds to

$$\psi_n^+ = \frac{l_m^2}{24 A_m^+} \left(\mathbf{C}_m^+ \cdot \left(9\mathbf{C}_m^+ - 15\mathbf{V}_{1,m} \right) + 7\left| \mathbf{V}_{1,m} \right|^2 - \mathbf{V}_{2,m} \cdot \mathbf{V}_{3,m} \right). \tag{7.38}$$

The integral over negative triangle gives us similar result, thus final relation for diagonal term is

$$\left\langle \boldsymbol{f}_m, \boldsymbol{f}_m \right\rangle = \frac{l_m^2}{24A_m^+}\left(\mathbf{C}_m^+ \cdot \left(9\mathbf{C}_m^+ - 15\mathbf{V}_{1,m}\right) + 7\left|\mathbf{V}_{1,m}\right|^2 - \mathbf{V}_{2,m} \cdot \mathbf{V}_{3,m}\right) + \frac{l_m^2}{24A_m^-}\left(\mathbf{C}_m^- \cdot \left(9\mathbf{C}_m^- - 15\mathbf{V}_{4,m}\right) + 7\left|\mathbf{V}_{4,m}\right|^2 - \mathbf{V}_{2,m} \cdot \mathbf{V}_{3,m}\right). \tag{7.39}$$

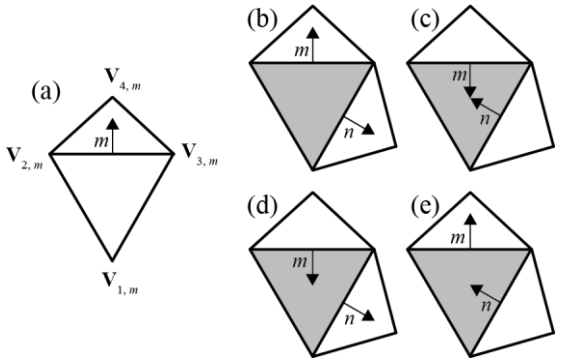

Figure 7-3: Sketch of the m-th RWG function (a) and of an overlap (b, c, d, e) between the m-th and the n-th RWG function. An arrow denotes the orientation of the RWG functions. The vertices are denoted by corresponding radius vectors $\mathbf{V}_m$*. The grey colour represents the overlap region.*

7.8. Excitation matrix Q in RWG basis

In our case of RWG basis scalar product in (3.4) is defined as

$$\mathbf{q}_n = \int_S \boldsymbol{f}_n(\boldsymbol{r}) \cdot \boldsymbol{E}(\boldsymbol{r})\,\mathrm{d}S = \frac{l_n}{2A_n^+}\int_{\Delta_n^+} \boldsymbol{\rho}_n^+ \cdot \boldsymbol{E}(\boldsymbol{r})\,\mathrm{d}S + \frac{l_n}{2A_n^-}\int_{\Delta_n^-} \boldsymbol{\rho}_n^- \cdot \boldsymbol{E}(\boldsymbol{r})\,\mathrm{d}S, \tag{7.40}$$

where $\mathbf{q}^{[N\times 1]}$ is column of matrix $\mathbf{Q}^{[N\times 6]}$, every column is for one wave. Since the scale of triangles is assumed to be smaller than the scale of the important spatial variations of the incident electromagnetic field, we can write

$$\mathbf{q}_n \approx \frac{l_n}{2A_n^+}\boldsymbol{E}\left(\mathbf{C}_n^+\right) \cdot \int_{\Delta_n^+} \boldsymbol{\rho}_n^+\,\mathrm{d}S + \frac{l_n}{2A_n^-}\boldsymbol{E}\left(\mathbf{C}_n^-\right) \cdot \int_{\Delta_n^-} \boldsymbol{\rho}_n^-\,\mathrm{d}S. \tag{7.41}$$

The integrals in (7.41) are the same as integrals in (7.15), thus

$$\begin{aligned}\int_{\Delta_n^+} \boldsymbol{\rho}_n^+ \,\mathrm{d}S &= \frac{l_n}{2}\boldsymbol{\rho}_n^+\left(\mathbf{C}_n^+\right),\\ \int_{\Delta_n^-} \boldsymbol{\rho}_n^- \,\mathrm{d}S &= \frac{l_n}{2}\boldsymbol{\rho}_n^-\left(\mathbf{C}_n^-\right).\end{aligned} \tag{7.42}$$

Putting all together

$$\mathbf{q}_n \approx \frac{l_n}{2}\left(\boldsymbol{E}\left(\mathbf{C}_n^+\right)\cdot\boldsymbol{\rho}_n^+(\mathbf{C}_n^+) + \boldsymbol{E}\left(\mathbf{C}_n^-\right)\cdot\boldsymbol{\rho}_n^-(\mathbf{C}_n^-)\right) \tag{7.43}$$

and we obtained one column of excitation matrix **Q**. Then we repeated this procedure for every six waves and we finally obtained the excitation matrix.

8. Bibliography

[1] J. D. Jackson, Classical Elektrodynamics, 3 ed., John Wiley, 1998.

[2] S. A. Schenlkunoff and H. T. Friis, Antennas: Theory and Practice, John Wiley, 1952.

[3] C. R. Simovsky, "On electromagnetic charakterization and homogenization of nanostructured metamaterials," *Journal of Optics,* vol. 13, no. 1, 2011.

[4] B. A. Munk, Frequency Selective Surface: Theoty and Design, John Wiley, 2000.

[5] A. Sihvola, T. K. Sarkar and B. Kolundzija, "From radar cross section to electrostatics," *IEEE Transactions on Antennas and Propagation,* vol. 3, no. 1, pp. 324-327, 2004.

[6] A. D. Yaghjian and H. R. Stuart, "Lower bounds on the Q of electrically small dipole antennas," *IEEE Transaction and Antennas Propagation,* vol. 58, no. 10, pp. 3114-3121, 2010.

[7] R. E. Collin, Field Theory of Guided Waves, New York: IEEE, 1990.

[8] S. Tretyakov, Analytical modeling in applied electromagnetics, Artech House, 2003.

[9] A. Sihvola, P. Ylä-Oijala, S. Järvenpää and J. Avelin, "Polarizabilities of Platonic Solids," *IEEE Transactions on Antennas and Propagation,* vol. 52, no. 10, pp. 2226-2233, September 2004.

[10] J. Helsing and K. M. Perfekt, "On the polarizability and capacitance of the cube," *Applied and Computational Harmonic Analysis,* vol. 34, pp. 445-468, 2013.

[11] S. B. Cohn, "The electric polarizability of apertures of arbitrary shape," *Proceedings of the IRE,* vol. 40, p. 1069, 1952.

[12] J. Reinert and A. F. Jacob, "Theoretical and experimental waveguide characterization of small wire scatterers," *IEEE Transactions on Microwave Theory and Techniques,* vol. 7, no. 49, pp. 1266-1269, 2001.

[13] L. Jelinek, J. D. Baena, R. Marques and J. Zehentner, "Direct polarisability extraction method," *European Microwave Conference,* p. 983, 2006.

[14] A. D. Scher and E. F. Kuester, "Extracting the bulk effective parameters of a metamaterial via the scattering from a single planar array of particles," *Metamaterials,* no. 3, pp. 1-36, 2009.

[15] S. M. Rao, D. R. Wilton and A. W. Glisson, "Electromagnetic Scattering by Surface of

Arbitrary Shape," *IEEE Transactions on Antennas and Propagation,* vol. 30, no. 3, pp. 409-418, May 1982.

[16] R. F. Harrington, Time-Harmonic Electromagnetic Fields, John Wiley - IEEE Press, 2001.

[17] R. F. Harrington, Field Computation by Moment Methods, John Wiley-IEEE Press, 1993.

[18] The MathWorks, Inc., *MATLAB,* The MathWorks, Inc., 1994-2016.

[19] MSC Software Corporation, *MSC Nastran.*

[20] R. Marques, F. Medina and R. Rafii-El-Idrissi, "Role of bianisotropy in negative permeability and left-handed metamaterials," *Physical Review B,* vol. 65, 2002.

[21] R. Marques, F. Mesa, J. Martel and F. Medina, "Comparative analysis of edge- and broadside- coupled split ring resonators for metamaterial design - theory and experiments," *IEEE Transactions on Antennas and Propagation,* vol. 51, pp. 2572-2581, 2003.

[22] R. Marques, L. Jelínek, M. J. Freire, J. D. Baena and M. Lapine, "Bulk metamaterials made of resonant rings," *Proceedings of the IEEE,* vol. 99, pp. 1660-1668, 2011.

[23] C. A. Balanis, Antenna Theory Analysis and Design, 3 ed., John Wiley, 2005.

[24] R. F. Harrington, "Matrix methods for field problems," *IEEE,* vol. 2, no. 55, 1967.

[25] P. O. Perrson, "Distmesh," February 2005. [Online]. Available: http://persson.berkeley.edu/distmesh/. [Accessed January 2016].

[26] W. C. Gibson, The Method of Moments in Electromagnetics, Chapman and Hall/CRC, 2007.

[27] S. N. Makarov, Antenna and EM Modeling with MATLAB, New York: John Wiley, 2002.